Micromechanical Simulation of the Deformation and Fracture of Polymer Blends

Gavin A. Buxton and Anna C. Balazs*

Department of Chemical and Petroleum Engineering, University of Pittsburgh, Pittsburgh, Pennsylvania 15261

Received July 26, 2004; Revised Manuscript Received October 25, 2004

ABSTRACT: We couple morphological studies of binary, immiscible blends with mechanical studies of deformation and fracture to determine the influence of the blend composition on the initiation and propagation of cracks in polymeric materials. The Cahn−Hilliard (CH) method is employed to simulate the structural evolution of the molten AB blend. We assume that the material undergoes a rapid quench to yield a solid whose microstructure is given by the CH approach. The output from these CH simulations serves as the input to a dynamic lattice spring model (LSM), a micromechanical model that consists of a three-dimensional network of springs, which connect regularly spaced mass points. Within the LSM, the A and B phases, as well as the interfacial regions, are assigned distinct spring constants, thereby allowing us to model a blend of a compliant and a stiff polymer. With the application of a tensile deformation, the heterogeneous microstructures give rise to complex local elastic fields. Using an energy-based fracture criterion, we selectively remove springs from this system and thereby simulate the initiation and propagation of cracks within the material. By varying the relative stiffness and toughness of the phases, we determine how these characteristics affect the growth of the cracks. We also consider systems where the interface between the different species is mechanically weak, and consequently, fracture occurs through the decohesion of the different polymer domains. In all the systems considered here, we find that "clustering effects", which are due to interactions between neighboring domains, play a major role in dictating where incipient fracture occurs. Through these studies, we can correlate the complex morphologies within the blend to the mechanical performance of the solid materials.

1. Introduction

An effective and relatively inexpensive way to create new structural materials is to form blends of already existing polymers. The overall properties of such blends can be tailored to exploit the desirable features of the individual components.[1] For example, the toughness of a stiff, brittle polymer can be improved through the addition of a compliant polymer; the compliant polymer also becomes stronger and stiffer because of the presence of the brittle component.[2] However, most polymer pairs are immiscible, and the mixtures phase separate into complex heterogeneous structures. Different structures are obtained depending upon the relative composition of the blend. For a binary, immiscible blend, either one polymer is dispersed within a matrix of the other or the mixture forms bicontinuous networks, which percolate across the material.[3] These complex morphologies, as well as a disparity between the mechanical properties of the two phases, can result in complicated stresses, strains, and fracture phenomena within the blend. In this study, we use a computational model to investigate both the deformation and rupture of these materials and thereby obtain further insight into the nature of fracture in brittle polymer blends.

To obtain the morphologies of polymer blends for a range of compositions, we employ the Cahn−Hilliard (CH) model.[4,5] The CH model is a computationally efficient method of capturing the diffusive nature of phase separating fluids. This makes the method ideal for simulating polymer melts where, due to their high viscosity, hydrodynamic interactions play a negligible part in the morphological evolution. The three-dimensional simulations of polymer blend spinodal decomposition and domain growth result in spatially heterogeneous structures, which can be directly used as the input to a micromechanical model.

The micromechanical model utilized here is the dynamic lattice spring model (LSM). The LSM consists of a lattice network of springs. Through the appropriate choice of spring constants, the model can accurately recover continuum elastic behavior.[6,7] The strength of the LSM approach lies in its ability to simulate complex heterogeneous systems in a computationally efficient manner. In particular, the LSM has been shown to accurately capture the elastic fields that correspond to Eshelby's well-known theoretical solutions for the elastic behavior of inhomogeneous materials[7] and has been used to simulate the deformation of multiparticulate systems.[8−10] Furthermore, the LSM has also been used to simulate the deformation of polymer blends of various compositions (and thus morphologies).[11]

Through the selective removal of springs, the LSM can be extended to simulate the initiation and propagation of quasi-static cracks. In this manner, LSMs have been used to simulate the statistical nature of material failure[12,13] and the failure of particulate composites.[14,15] However, to capture the dynamics of elastic waves and dynamic crack propagation, one must employ a dynamic LSM. The dynamic LSM consists of regularly spaced mass points that are connected by a lattice of springs. These masses represent mesoscopic portions of the solid material; the springs are connected such that the system recovers linear elasticity theory (in a manner similar to the quasi-static LSM). The positions and velocities of the mass points are obtained through the integration of Newton's equation of motion, and in this way, the model yields the dynamic properties of the elastic

* Corresponding author: e-mail balazs1@engr.pitt.edu.

10.1021/ma048470r CCC: $30.25 © 2005 American Chemical Society
Published on Web 12/30/2004

material. The dynamic LSM has been used to simulate the deformation and fracture of brittle polymers.[16,17] In studies of thin films, the LSM results show good agreement with experimental findings on the crack velocity and crack tip branching.[18]

Recently, we simulated the dynamic fracture of polymer blends processed under shear and found that the anisotropic orientation of the sheared morphologies led to anisotropic fracture properties.[19] However, in the previous study, differences in the elastic properties of the two components were not taken into consideration. It should be noted that polymers are often blended to enhance the composite stiffness or toughness, for which an elastic disparity between the two phases is a requirement. Therefore, here, we consider the deformation and fracture of polymer blends where one component is both stiffer and weaker than the other. We also assume that the polymers are linear elastic and that they fail irreversibly via an elastic energy-based fracture criterion. This restricts our studies to brittle polymers at a length scale larger than microscopic phenomena, such as shear yielding and crazing. It should be noted that atomistic simulations are required to accurately capture such microscopic phenomena. For example, Rottler and Robbins use molecular dynamic simulations to simulate the molecular level processes during craze nucleation, widening, and eventual breakdown.[20,21] However, the largest volume accessible to atomistic simulations is limited to roughly 100 nm^3. Continuum models have been used in attempts to simulate regions of crazing through the inclusion of either locally anisotropic spring networks[22,23] or special finite elements that are nonlinear and highly anisotropic.[24] Such continuum models, however, involve a priori assumptions regarding the location and orientation of the crazes. We, therefore, limit our study to linear elastic and perfectly brittle polymers and neglect such microscopic phenomena.

It is worth noting that one can incorporate nonlinear behavior into the LSM.[7,9] For example, viscoelasticity can be included by introducing a Kelvin unit, which is an elastic component that is connected in parallel with a viscous component. The Kelvin unit lies in series with each elastic spring. This configuration allows an instantaneous elastic deformation to be obtained while enabling full recovery of strain upon removal of the applied stress. In previous quasi-static studies,[9] we adopted this approach to contrast the elastic and viscoelastic response of particle-filled polymeric composites to a tensile deformation. In these more complex dynamical studies, we currently focus on elastic behavior; future studies will concentrate on developing a dynamic, nonlinear model for the deformation and fracture of polymer blends.

It should also be noted that similar morphological models have been extended to ternary mixtures, where the third component can compatibilize the binary blend.[25] Recently, a lattice Boltzmann method was used to simulate a ternary mixture where the compatibilizer is formed reactively in situ.[26] It is possible to integrate the LSM with these morphological studies and thereby simulate the mechanical bahavior of compatibilized polymeric systems.

The following section details the computational methods used in this study. First, we briefly describe the CH model, which is used to gain structural information regarding the morphologies of polymer blends. Second, we describe the dynamic LSM for simulating the deformation and fracture of highly heterogeneous systems.

2. Methodology

2.1. Morphology Model. We describe the evolution of an A/B polymer blend through the coarse-grained Cahn−Hilliard (CH) approach. Here, we consider mesoscopic length and time scales, where details of molecular motions can be neglected, implying that a continuum description is appropriate. The system is characterized by the order parameter $\Psi(\mathbf{r})$, which is the difference in concentration between the two components, $\Psi(\mathbf{r}) = \Phi_A(\mathbf{r}) - \Phi_B(\mathbf{r})$, where $\Phi_A(\mathbf{r})$ and $\Phi_B(\mathbf{r})$ are the local volume fractions of components A and B, respectively. The equilibrium order parameter for the A-rich (B-rich) phase corresponds to $\Psi = \Psi_{eq}$ ($-\Psi_{eq}$), and here we take $\Psi_{eq} = 1$. The evolution of this order parameter is described by the following equation:[4,5]

$$\frac{\partial \Psi}{\partial t} = M\nabla^2 \frac{\delta F}{\delta \Psi} + \xi \tag{1}$$

where M is the kinetic coefficient (mobility) of the order parameter field and ξ is a noise term. The effects of noise have been found to accelerate the early time dynamics but have little effect on the domain growth (and, hence, the late stage morphologies);[27] therefore, we set this noise term to zero in this study.

The total free energy is given by $F = \int F_L + F_G \, d\mathbf{r}$, where the integration is over the volume of the system. The local energy term adopted in the current study is given by

$$F_L = -A \log(\cosh(\Psi)) + \frac{1}{2}\Psi^2 \tag{2}$$

making it energetically favorable for either $\Psi = \Psi_{eq}$ or $\Psi = -\Psi_{eq}$. The gradient energy term is

$$F_G = \frac{D}{2}(\nabla\Psi)^2 \tag{3}$$

which makes the creation of interfaces between A-rich and B-rich regions energetically unfavorable. The parameters A and D are material specific.

The cell dynamical systems (CDS) method[28,29] is used to discretize and numerically solve the above CH equation. The employment of CDS (rather than a conventional finite-difference scheme) significantly reduces the computational expense of the simulations and thus provides a computationally efficient model for the evolution of polymer melts. The discrete equations are of the form

$$\Psi(\mathbf{r}, t+1) = G[\Psi(\mathbf{r}, t)] - \langle\langle G[\Psi(\mathbf{r}, t)] - \Psi(\mathbf{r}, t)\rangle\rangle \tag{4}$$

where a hyperbolic tangent is included in the function G (although the results are insensitive to this choice of mapping[28]):

$$G[\Psi(\mathbf{r}, t)] = A \tanh(\Psi) + D(\langle\langle\Psi(r, t)\rangle\rangle - \Psi(r, t)) \tag{5}$$

In the current simulations, the constants in eq 5 are fixed at the following values: $A = 1.3$ and $D = 0.5$. Our simulations, therefore, correspond to a deep quence and a highly immiscible mixture.[28] (Note that the time step in the CDS is assumed to be of order $\Delta x^2/M$.[28,29]) The

operator $\langle\langle\bigstar\rangle\rangle$ indicates an isotropic spatial average over the neighboring nodes, and $[\langle\langle\bigstar\rangle\rangle - \bigstar]$ can be considered as a discrete generalization of the Laplacian. In three dimensions, the spatial average on a cubic lattice can be given by

$$\langle\langle\bigstar\rangle\rangle = \frac{6}{80}\sum_{NN}\bigstar + \frac{3}{80}\sum_{NNN}\bigstar + \frac{1}{80}\sum_{NNNN}\bigstar \qquad (6)$$

where *NN*, *NNN*, and *NNNN* represent the nearest, next-nearest, and next-next-nearest neighbors, respectively.[30]

The morphologies obtained from the CH model are assumed to remain unchanged upon quenching to a temperature below the melt transition temperature. Below, we detail the model used to probe the mechanical properties of the resulting polymeric solid.

2.2. Micromechanical Model. We use a dynamic lattice spring model (LSM) to simulate the deformation and fracture of the polymer blends. The LSM is a numerical technique for discretizing linear elasticity theory and consists of a network of springs that connect regularly spaced lattice sites or nodes. The energy associated with the ith node is given by[7]

$$E_i = \frac{1}{2}\sum_j (\mathbf{u}_i - \mathbf{u}_j)\cdot\mathbf{M}_{ij}\cdot(\mathbf{u}_i - \mathbf{u}_j) \qquad (7)$$

where the summation is over all nearest- and next-nearest-neighboring nodes. Here, $\mathbf{u}_i$ is the displacement of the ith node from its original position and $\mathbf{M}_{ij}$ is a matrix containing the force constants (stiffnesses) for a spring connecting nodes i and j. Two different types of force constants, central and noncentral, are assigned to each spring. The central force constant energetically penalizes spring extension, while the noncentral force constant penalizes the rotation of springs from their original orientation. The Young's modulus, E, and Poisson's ratio, ν, are related to the force constants by the following equations[7]

$$E = \frac{5K(2K + 3C)}{4K + C} \qquad \nu = -\frac{K - C}{C + 4K} \qquad (8)$$

where K and C are the central and noncentral force constants, respectively.

Because of the harmonic form of the energy in eq 7, the elastic forces are a linear function of the displacements. The force acting on the ith node, due to the local displacements of its neighboring nodes, is given by

$$\mathbf{F}_i = \sum_j \mathbf{M}_{ij}\cdot(\mathbf{u}_i - \mathbf{u}_j) \qquad (9)$$

To capture the dynamics of this system, we must integrate Newton's equation of motion

$$M_i\frac{\partial^2\mathbf{u}_i}{\partial t^2} = \mathbf{F}_i - \Theta\frac{\partial\mathbf{u}_i}{\partial t} \qquad (10)$$

where M_i is the mass associated with the ith node. The Stokes drag term, with coefficient Θ, accounts for dissipation through viscous damping. The most commonly used time integration algorithm is the Verlet algorithm.[31] Here, we use the velocity Verlet algorithm[32] in order to capture the velocities (necessary for including viscous damping). The velocity Verlet scheme takes the positions, velocities, and accelerations at time t to obtain the same quantities at time $t + \Delta t$ in the following way:

$$\mathbf{u}_i(t + \Delta t) = \mathbf{u}_i(t) + \mathbf{v}_i(t)\Delta t + \frac{1}{2}\mathbf{a}_i(t)\Delta t^2$$

$$\mathbf{v}_i\left(t + \frac{\Delta t}{2}\right) = \mathbf{v}_i(t) + \frac{1}{2}\mathbf{a}_i(t)\Delta t$$

$$\mathbf{a}_i(t + \Delta t) = -\frac{\mathbf{F}_i(t)}{M_i} - \Theta\mathbf{v}_i\left(t + \frac{\Delta t}{2}\right)$$

$$\mathbf{v}_i(t + \Delta t) = \mathbf{v}_i\left(t + \frac{\Delta t}{2}\right) + \frac{1}{2}\mathbf{a}_i(t + \Delta t)\Delta t \qquad (11)$$

where $\mathbf{v}_i$ and $\mathbf{a}_i$ are the velocity and acceleration, respectively, of the ith node. The mass and central force constants are taken to be unity; the noncentral force constant is set to zero (resulting in a Poisson's ratio of 1/4). The viscous damping constant, Θ, is set to 1/4, resulting in a material where elastic waves are underdamped. The above equations allow us to capture the elastic deformation and dynamic behavior of the material.

To introduce material degradation, we selectively remove springs from the system. A surface is randomly created, and hence a cluster of springs that cross this surface are broken, depending upon the energy that would be released through the creation of this surface. Clusters of springs are removed in order to create well-defined surfaces in a more isotropic manner.[19] Crack growth can generally be considered to occur if the energy required to create a new crack surface can be delivered by the system.[33] Here, we adopt an energy-based fracture criterion, which penalizes both tension and shear deformations.[34]

To determine which fracture surface is to be created, a rate of failure $p_i(t)$ of a surface i at time t is introduced

$$p_i(t) \propto \left[\frac{(E_i(t) - w_i)}{w_i}\right]^\beta \qquad (12)$$

where $E_i(t)$ is the local energy that is stored in the springs that across the ith potential fracture surface at time t. The minimum value of elastic energy at which fracture can occur is w_i, referred to as the lower bound toughness. The modulus β allows for a nonlinear relationship between damage rate and elastic energy field. The difference between the energy stored across the fracture surface and the lower bound toughness $(E_i(t) - w_i)$ is normalized by the lower bound toughness. Thus, if we make the toughness of the B phase to be 50% the toughness of the A phase, then both phases will have the same probability of fracture when the elastic energy stored in the B phase is half that stored in the A phase. Assuming that the damage is to occur somewhere in the system, the probability of failure, $P_i(t)$, occurring at a given surface i is the rate associated with surface i relative to the total rate of damage occurring throughout the material, i.e., $P_i(t) = p_i(t)/\sum_j p_j(t)$, where the sum is over all surfaces.[35] A surface is chosen to fracture from the cumulative probability, and therefore, selection takes into consideration the correct probability weightings. The cumulative probability is defined as

$$c_i(t) = \sum_{j\le i} P_j(t) \qquad (13)$$

and spans the range from 0 to 1. The average time interval for this failure event to occur is[35]

$$\Delta t = \frac{1}{\sum_j p_j(t)} \tag{14}$$

This time step is used to update the expressions in eq 11.

To initiate fracture, a constant strain rate is applied to the sample. An initial time step is introduced, Δt_0, and the strain is initially increased at each iteration by $\dot{u}\Delta t_0$, where $\dot{u}$ is the constant strain rate. If the average time interval for fracture to occur (eq 14) is smaller than Δt_0, then a surface is created. In particular, the ith surface chosen to fail is the surface for which $c_i(t) < RND[0, 1] < c_{i+1}(t)$, where $RND[0, 1]$ is a random number between 0 and 1. If the value of Δt from eq 14 is greater than Δt_0, then $\Delta t = \Delta t_0$, and this value is used to update the applied strain and the dynamic equations with no fracture occurring. Therefore, the creation of fracture surfaces depends on the correct probability weightings (eq 12), and the relaxation of material surrounding the propagating crack tip takes into consideration the average time interval over which the crack grows. The material deforms and fractures in this manner until the crack has propagated the length of the system and two separate pieces of the material remain.

We take the morphologies from the CH simulations and incorporate them directly into the LSM simulations. Along the boundaries of the simulation box, in the tensile direction, we add additional regions of pure B polymer (thickness of 5 lattice sites) where fracture is prohibited. This ensures cracks do not run off the edge of the simulation domains. Fracture is initiated in the heterogeneous central regions, where elastic energy concentrations are present. In this manner, we can investigate the effects of the mesoscale morphology on the ultimate fracture characteristics of the material.

3. Results and Discussion

3.1. Morphology: Phase-Separated Polymer Blends. The system size considered here is $L^3 = 64^3$, where L is the length of the cubic simulation box in lattice sites. The simulations start with a homogeneous mixture of both A and B species. These species form individual A and B domains, and the subsequent domain growth obeys the Lifshitz−Slyozov law, scaling with time t as $t^{1/3}$. Typical late stage morphologies (at time $t = 2000$) are shown in Figure 1. Isosurfaces with a constant order parameter of $\Psi = 0$, which separate A-rich from B-rich regions, are depicted in red. For clarity, the regions where the A phases cross the simulation boundaries are shown as black "caps". Blend morphologies ranging from dispersed to bicontinuous are shown. A system of 30:70 composition is depicted in Figure 1a, which clearly shows the dispersed morphology. The minority phase is isolated and dispersed as droplets within a matrix of the majority phase. Figure 1b depicts a system of 40:60 composition in which the A phase consists of a network of connecting domains that span the system. This represents a bicontinuous structure as both phases percolate. A system of 50:50 composition is shown in Figure 1c where again the domains are bicontinuous, but in this case the size of the A and B domains are equivalent.

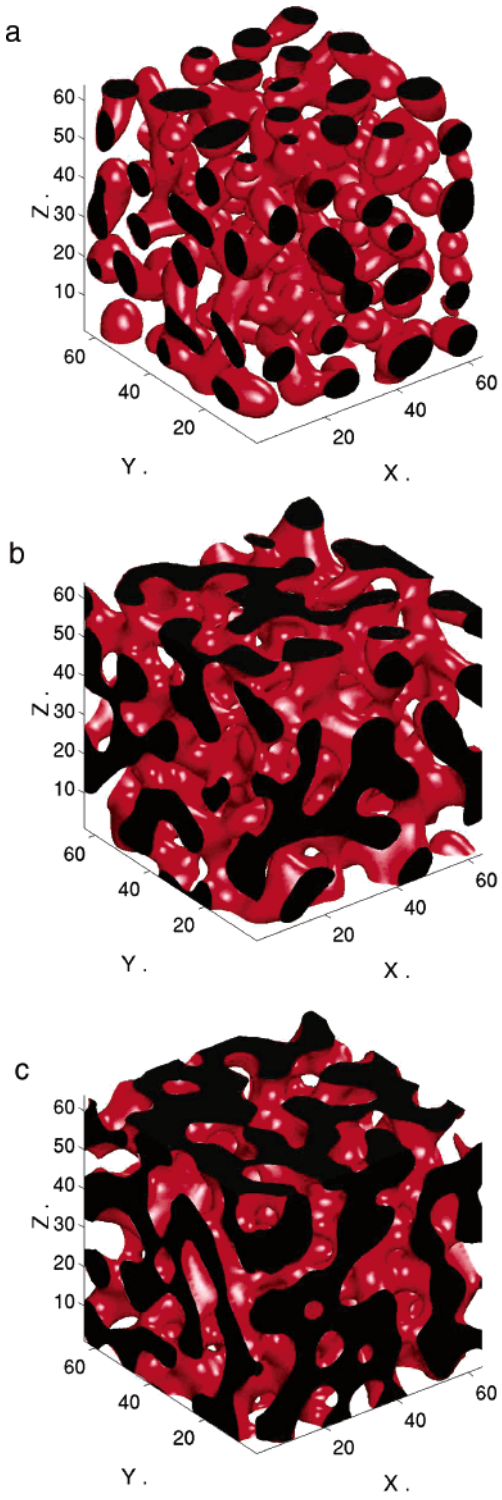

Figure 1. Structural output from the CH model showing typical late stage morphologies. The composition is (a) 30:70, (b) 40:60, and (c) 50:50 and depicts a variation from a dispersed to a bicontinuous structure.

The interfacial area can be calculated using the broken bond method and is inversely proportional to the domain size. The total interfacial area is defined as $\Lambda = N_x + N_y + N_z$, where N_i is the number of broken bonds (pairs of nearest-neighbor sites with opposite signs of Ψ) in the ith direction. Figure 2 shows the total interfacial area as a function of time (during the domain growth period of the simulations) for systems of 30:70, 40:60, and 50:50 composition. Data are averaged over 20 independent runs. The interfacial area of the bicon-

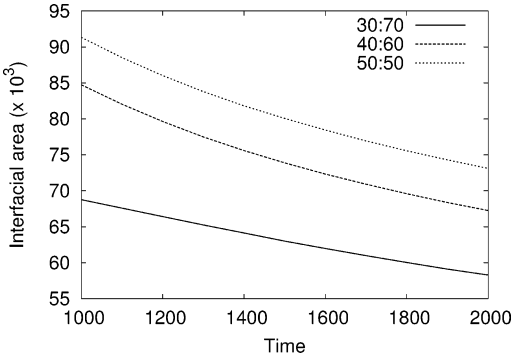

Figure 2. Interfacial area as a function of time for different polymer blend compositions. Data are presented during the domain growth regime and are averaged over 20 independent runs.

tinuous system of 50:50 composition is found to be roughly 25% greater than that of the dispersed system.

We can now take these morphologies and feed them directly into a LSM simulation. By assigning a different stiffness to each of the domains, the complex elastic deformation fields associated with these polymeric systems can be examined. Furthermore, the fracturing of the polymeric material at regions of large elastic deformation can also be investigated.

3.2. Mechanical Properties: Deformation and Fracture. Using the dynamic LSM, we deform the above systems through the application of a strain, at the system boundaries, along the x-direction. The strain is gradually increased at a constant rate. (Our strain rate in dimensionless units is taken to be $\dot{u} = 1.56 \times 10^{-4}$; this corresponds to a high strain rate that is $<10^4$ s^{-1} in real units.[36]) We initially consider the elastic fields of the various polymer systems after the systems have been extended up to a global strain of approximately 3%. The spring constant of the pure B phase, K_B, is taken to be 10 times stiffer than K_A, the spring constant of the pure A phase; thus, the Young's modulus of the B polymer is 10 times greater than that of the A polymer. (This represents a relatively large elastic disparity for polymeric systems, such as the difference between low-density polyethylene and nylon-66.[40]) The interfacial regions are assigned intermediate spring constants through a simple linear rule of mixture. This disparity in elastic moduli results in complex elastic fields throughout the deformed systems. We show the elastic fields in Figures 3−5 as orthogonal contour plots that slice through the 3D systems. The interfaces between A-rich and B-rich phases ($\Psi = 0$) are marked with single black contour lines, which are superimposed over the elastic field contours.

Figure 3 depicts the normal stress fields (σ_{xx}, where σ_{ij} is the stress tensor) for AB blends with the following compositions: (a) 70:30, (b) 50:50, and (c) 30:70. This means that we consider systems that range from the stiffer phase being dispersed as droplets in a more compliant matrix, through a bicontinuous system, to the softer phase being dispersed in a stiff matrix. The maximum stress in Figure 3 is ~0.5 in dimensionless units; if we compare the corresponding dimensionless Young's moduli to the typical order of magnitude that characterizes the Young's moduli for polymeric materials,[40] this value is equivalent to a stress of ~50 MPa.[36] Figure 3a shows the stress field in a system where the minority phase is stiffer than the matrix, and therefore, there are stress concentrations in the minority phases.

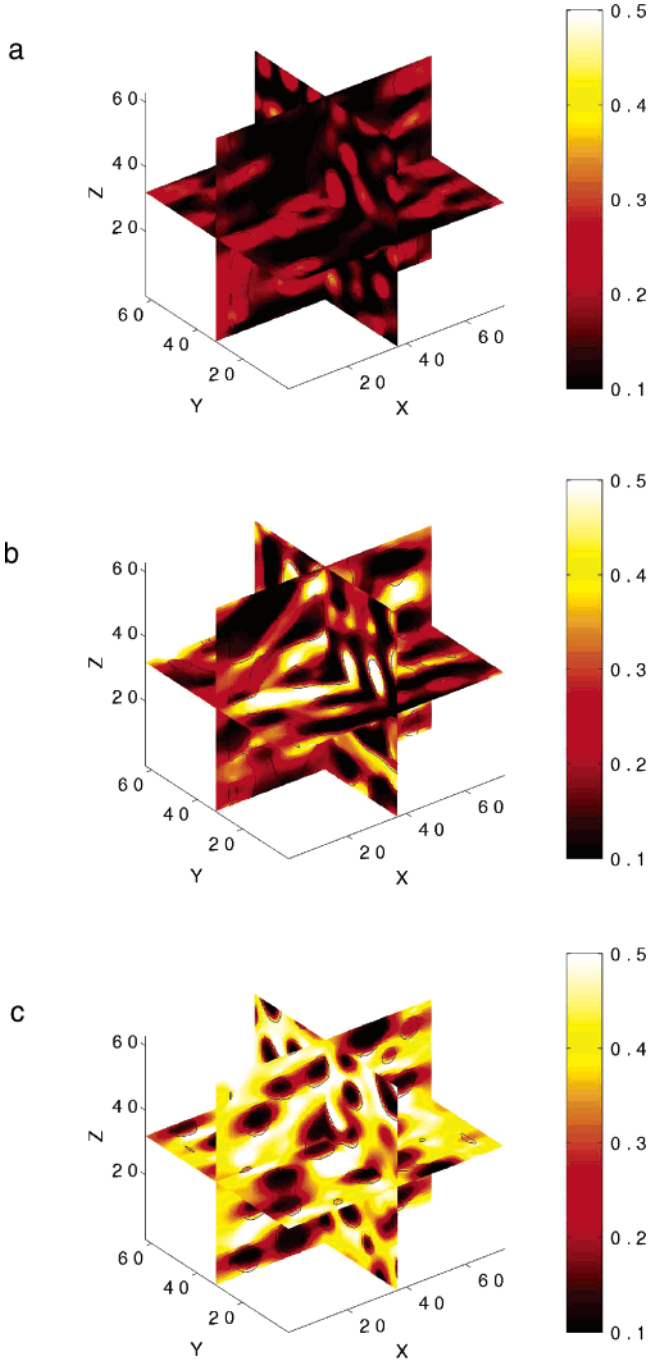

Figure 3. Normal stress fields for systems of (a) 70:30, (b) 50:50, and (c) 30:70 compositions. The stress fields are presented as orthogonal contour plots dissecting the simulation domain. The stiffer polymer phase possesses a Young's modulus 10 times greater than that of the softer polymer phase.

These stress concentrations extend from the minority stiff phases, through the poles of the droplets (along the direction of the applied strain),[41] and into the soft matrix along the x-direction. Figure 3b depicts the stress field for a bicontinuous (50:50 composition) system. Again, the stress is predominantly concentrated in the stiffer phases. The overall stress in the system is increased because the same strain is applied as before, but now it is applied to a stiffer sample. Figure 3c shows the normal stress field for the system where the minority phase is soft and the majority matrix phase is stiffer. The higher stresses are again in the stiffer majority phase, and the softer minority phase sustains significantly lower stresses. The regions of lower stress in the

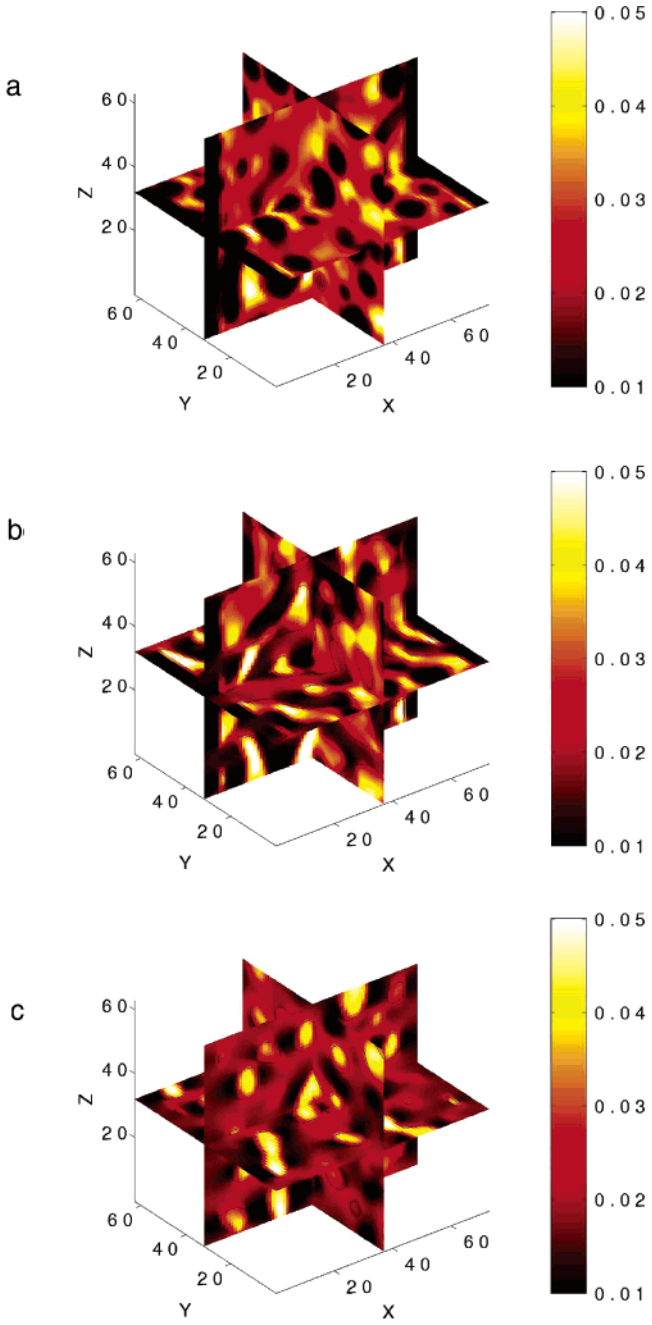

Figure 4. Normal strain fields for systems of (a) 70:30, (b) 50:50, and (c) 30:70 compositions. The strain fields are presented as orthogonal contour plots dissecting the simulation domain. The stiffer polymer phase possesses a Young's modulus 10 times greater than that of the softer polymer phase.

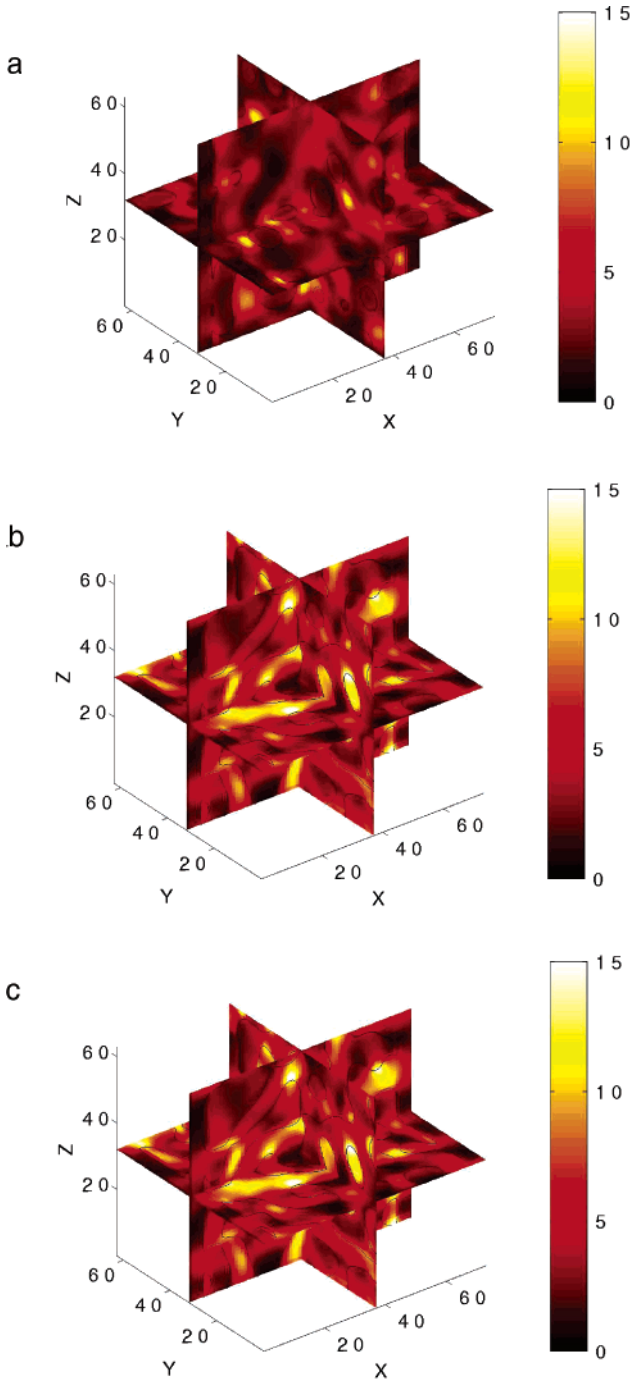

Figure 5. Elastic energy fields ($\times 10^{-3}$) for systems of (a) 70:30, (b) 50:50, and (c) 30:70 compositions. The elastic energy fields are presented as orthogonal contour plots dissecting the simulation domain. The stiffer polymer phase possesses a Young's modulus 10 times greater than that of the softer polymer phase.

softer minority phase extend into the stiff matrix at the poles of the droplets, especially when droplets are close together such that clustering effects occur. Furthermore, the largest stress concentrations in the majority phase are in regions near the interfaces with the minority soft phases in the equatorial plane (perpendicular to the direction of applied strain[41]). These stress concentrations are also subject to clustering effects and are especially high where droplets of the softer phase are close to each other, such that the regions of stress concentrations overlap.

In addition to calculating the stress fields, we can also obtain the normal strain fields (u_{xx}, where u_{ij} is the strain tensor). These are shown in Figure 4 for the following compositions: (a) 70:30, (b) 50:50, and (c) 30:70. Figure 4a shows the normal strain field in the system where the minority stiffer phase is dispersed in the majority softer phase. The stiffer droplets inhibit the deformation of the surrounding softer matrix in the equatorial plane (perpendicular to the direction of applied strain) but induce strain concentrations at the poles of the droplets (along the direction of applied strain). These strain concentrations are greatest when particles are within close proximity, such that the regions of high strain overlap. Figure 4b shows the normal strain field for the bicontinuous system (50:50 composition). The strain is generally greatest in the

more compliant polymer phase, especially in regions where the domain structure is elongated in a direction perpendicular to the direction of applied deformation. Figure 4c shows the normal strain field in a system of 30:70 composition in which the minority soft phase is dispersed within the stiffer majority phase. Again, the regions of greatest strain are almost exclusively within the softer polymer phase. Strain concentrations in the stiffer matrix phase occur near the equatorial plane of the dispersed droplets, while regions of relatively low strain lie at the poles of the droplets.

The utility of the above images can clearly be seen by comparing parts a and c of Figure 3 as well as parts a and c of Figure 4. The comparison allows one to readily visualize the extent to which the local mechanical response is affected by altering the relative ratio of the stiffer and softer components.

In the ensuing simulations, we utilize an energy-based fracture criterion. Therefore, it is useful to elucidate the regions of high energy in these systems. The elastic energy is obtained from eq 7 and is equivalent to $H = {}^1/_2 u_{ij}\sigma_{ij}$, which couples both the strain, u_{ij}, and the stress, σ_{ij}, tensors. Figure 5 shows this elastic energy for systems with the following compositions: (a) 70:30, (b) 50:50, and (c) 30:70. The maximum elastic energy in Figure 5 is $\sim 15 \times 10^{-3}$ in dimensionless units; if we compare our dimensionless Young's moduli to typical values of Young's moduli for a range of polymers,[40] this corresponds to an energy density of $\sim$1500 kJ m^{-3}.[36] By referring back to Figures 3 and 4, we can obtain a greater understanding of the images in Figure 5 and comprehend the relative contributions of the stress and strain fields to the elastic energy. Figure 5a depicts the elastic energy field for a system where a minority stiff phase is dispersed in a softer matrix. The regions of high elastic energy are in the softer matrix at the poles of the droplets. The highest elastic energy is localized in regions between droplets that are aligned in the direction of applied deformation and where the strain concentrations about these droplets overlap (as can be seen in Figure 4a). It is in these regions where fracture might be expected to occur. Figure 5b shows the elastic energy field for the bicontinuous (50:50 composition) system. The regions of greatest elastic energy are in the stiffer phases; the softer phase essentially stretches the stiffer phases, especially in regions where the domain structures are oriented in the direction of applied deformation. It is in these regions, where the structure carries the most stress (see Figure 3b), that fracture might be expected to initiate in the 50:50 bicontinuous systems. The elastic energy field in a system in which the minority soft phase is dispersed in a matrix of majority stiffer material (30:70 composition) is shown in Figure 5c. The total energy absorbed in this system, after the application of a given global deformation, is noticeably higher than in the 70:30 system as it requires more energy to deform a stiffer system than it does to deform a softer system to the same level of deformation. In Figure 5c, the higher energy fields are generally found in the stiffer matrix phase in the equatorial plane about the droplets, as these easily deformable droplets are less capable of supporting the stress fields (see Figure 3c). The above deformation fields provide insight into where cracks are likely to initiate in these highly heterogeneous systems and also reveal why those regions are more vulnerable than others.

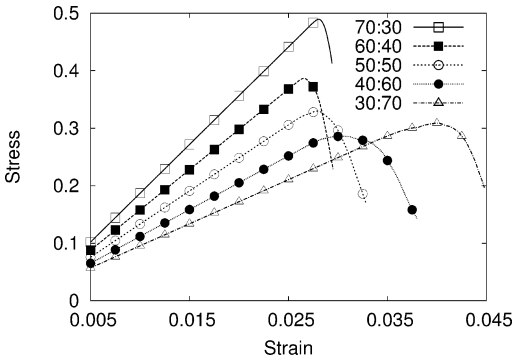

Figure 6. Stress−strain plots for systems of different compositions ranging from systems containing soft dispersed droplets in a stiff matrix, through bicontinuous systems, to systems containing stiff dispersed droplets in a soft matrix. The toughness of the stiffer phase is taken to be 50% that of the softer phase.

Having established the elastic fields and the elastic energy distribution in the material, we now apply our fracture criteria to the different samples to characterize fracture in these systems. The resultant stress−strain curves are shown in Figure 6, and the data are averaged over five independent runs. In the following discussion, when we refer to the toughness of a phase, we are using these terms in the context of eq 12 and the lower bound toughness parameter. For example, the B phase is considered to be 50% tougher than the A phase when w_B for the B phase (eq 12) is set to half the value of w_A for the A phase. For the A phase, we set $w_A = 0.1$, and thus, for the B phase, we have $w_B = 0.05$. The fracture criteria in the interfacial regions is initially set to an intermediate value of $w_I = 0.075$. The modulus in eq 12, β, is assigned the value of two, yielding a nonlinear response to the deformation of the system. The maximum in these stress−strain curves corresponds to the maximum stress that the system can sustain before the occurrence of catastrophic failure (the formation of one dominant crack). Surprisingly, the bicontinuous structures are neither relatively strong (maximum stress) nor tough (area under the curve). This is presumably due to the greater interfacial area in these blends, and therefore, a greater number of regions where significant elastic disparity occurs. It is at these regions where elastic field concentrations are found, and therefore, an elevated probability of failure is likely.

To isolate factors that influence the propagation of cracks in the material, we examine the effects of varying the difference in elastic moduli as well as the relative weakness of the stiffer phase. In particular, the stiffness of the B phase is considered to be either 2.5, 5, or 10 times greater than the A phase (where stiffness is set by the value of K_i, the corresponding spring constant), and the toughness of the B phase is considered to be a half or a quarter of the toughness of the A phase (w_B = 50% w_A or w_B = 25% w_A). Figures 7−9 show the number of broken bonds in the A phase (solid line), B phase (dashed line), and interfacial regions (dotted line) as a function of time; the data are averaged over five independent runs. For each composition, we consider six distinct systems, which correspond to the various stiffnesses and weaknesses of the B polymer relative to the A polymer. Figure 7 shows the results for the 70:30 composition. For the cases where the toughness of the B phase is 50% that of the A phase (w_B = 50% w_A), the system fractures predominantly in the A phase, and this becomes more pronounced as the elastic disparity

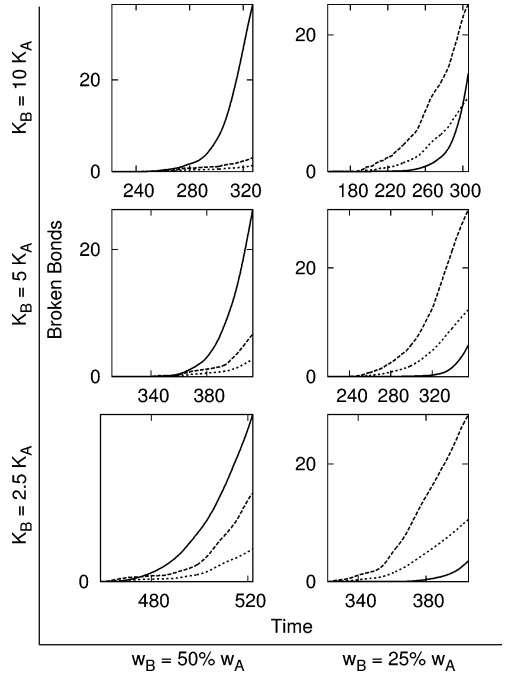

Figure 7. Number of broken bonds ($\times 10^3$) as a function of time for systems of 70:30 composition. Broken A bonds (solid lines), B bonds (dashed lines), and interfacial bonds (dotted) are presented for systems where the stiffness of the B polymer is 2.5, 5, and 10 times that of the A polymer, and the toughness of the B polymer is 50% and 25% that of the A polymer.

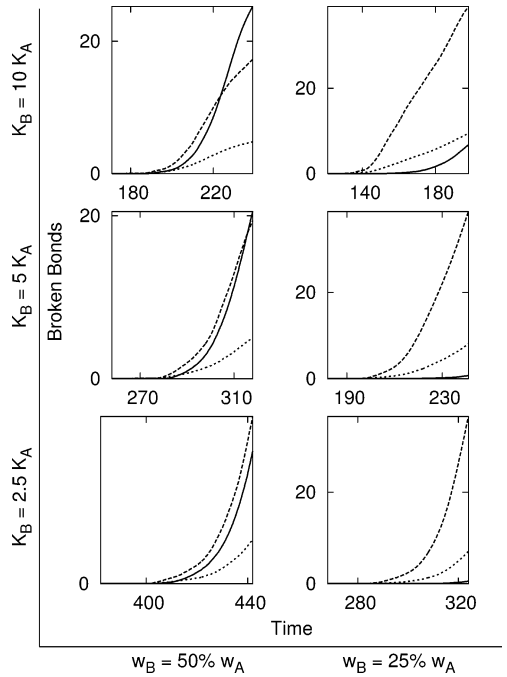

Figure 8. Number of broken bonds ($\times 10^3$) as a function of time for systems of 50:50 composition. Broken A bonds (solid lines), B bonds (dashed lines), and interfacial bonds (dotted) are presented for systems where the stiffness of the B polymer is 2.5, 5, and 10 times that the A polymer and the toughness of the B polymer is 50% and 25% that of the A polymer.

between the two phases is increased. However, for the cases where the B polymer is weakened even further ($w_B = 25\%\ w_A$), the weaker B phase is where fracture is initiated and predominantly propagates. Thus, even though the B phase is the minority phase, the most pronounced variation observed in this system is due to decreasing the toughness of this B component.

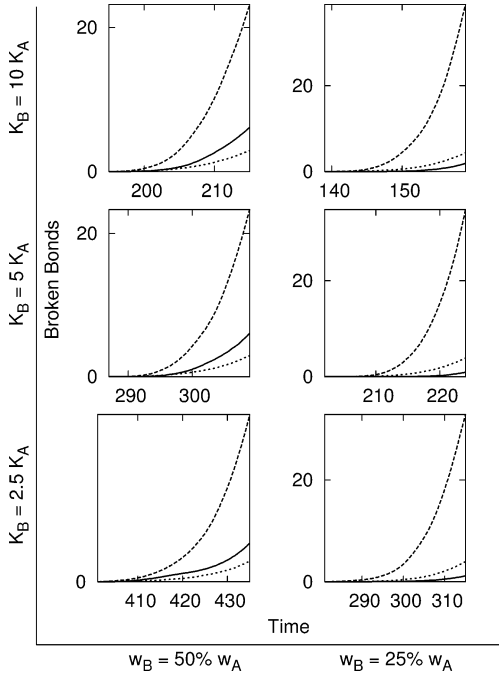

Figure 9. Number of broken bonds ($\times 10^3$) as a function of time for systems of 30:70 composition. Broken A bonds (solid lines), B bonds (dashed lines), and interfacial bonds (dotted) are presented for systems where the stiffness of the B polymer is 2.5, 5, and 10 times that the A polymer and the toughness of the B polymer is 50% and 25% that of the A polymer.

Figure 8 shows the regions of damage accumulation for the bicontinuous systems of 50:50 composition. In all of the bicontinuous cases considered here, fracture is initiated in the stiffer B phase. For systems where the toughness of the B polymer is quarter of that of the A polymer ($w_B = 25\%\ w_A$), the B phase fractures almost exclusively throughout the simulations. For the cases where the toughness of the B polymer is only half that of the A phase, fracture is still initiated in the B phase and occurs more in the B phase than in the A phase; however, now there is also significant damage in the A phase. Furthermore, as the disparity in the elastic moduli between the A and B phases is increased, there is a transition from the most damaged regions being in the B phase to the most damage being sustained in the A phase. Thus, in these systems, altering the modulus of the stiffer B phase has a dramatic effect on the fracture characteristics.

The damage accumulated in the systems of 30:70 composition is shown in Figure 9. The fracture in these systems is predominantly in the weaker B phase, and this observation is independent of the differences in either the elastic moduli or weakness for the systems considered here. For all the compositions considered, the time at which fracture occurred was earlier in the systems where the disparity in the elastic moduli was greater and hence the applied strain was lower (all systems where deformed under the same constant strain rate). This would imply that the local regions of elastic mismatch, and the large stress and strain concentrations that are produced by this mismatch, are primarily responsible for the initiation of fracture in these heterogeneous systems.

Another important characteristic that we can obtain from these calculations is the relative location of the onset of fracture in the different blends. We concentrate on the systems where $K_B = 10K_A$, and the toughness of

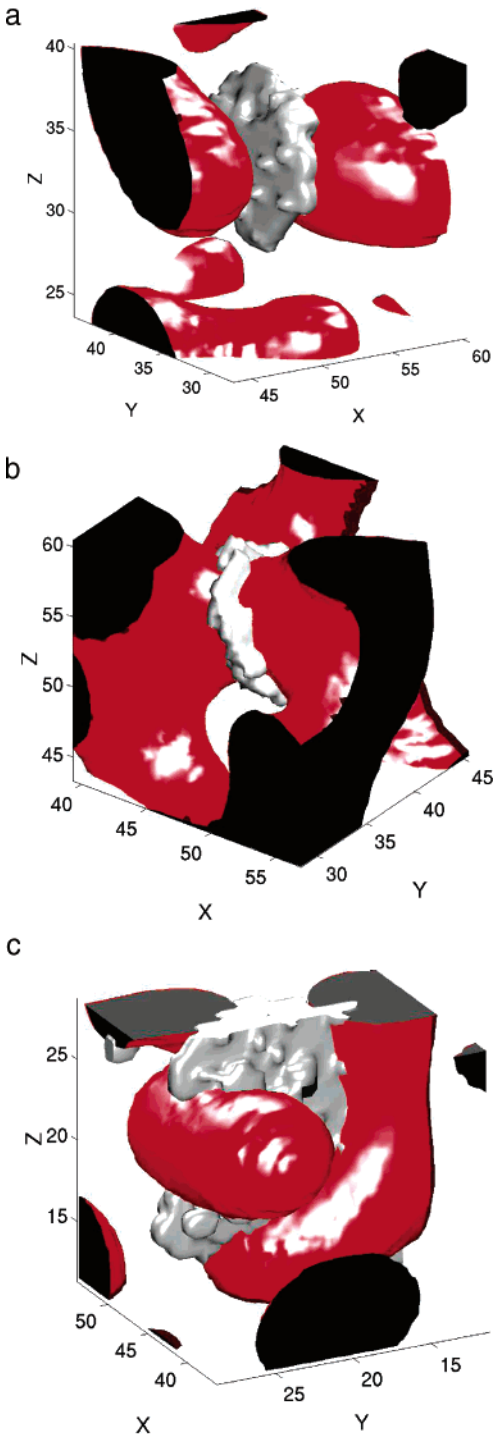

Figure 10. Graphical representation of a typical region of incipient fracture for a system where the stiffness of the B polymer is 10 times that of the A polymer and the toughness of the B polymer is 50% that of the A polymer. Systems of (a) 70:30, (b) 50:50, and (c) 30:70 composition are presented. Deformation is applied in the x-direction.

this stiffer B phase is half that of the A phase. A representative example of the initiation of fracture in a system of 70:30 composition is shown in Figure 10a. The boundary between the A and B polymers is shown as a red surface; black surfaces represent regions where the minority B phase crosses the system boundaries. The fracture surface is shown in gray, and only a small portion of the simulation is shown for clarity. A microcrack has appeared in between two droplets of stiff B polymer. The elastic energy fields in Figure 5a depict regions between stiff droplets that are aligned in the tensile direction (x-direction) and indicate concentrations of high elastic energy at these sites. Concentrations arising from such clustering effects result in the initiation of a crack, which then propagates in the plane perpendicular to the tensile direction. It should be noted, however, that the systems where the B polymer is even weaker ($w_B = 25\%\ w_A$) result in fracture initiating in the brittle droplets (see Figure 7).

Figure 10b shows the initiation of fracture in a bicontinuous system of 50:50 composition. The elastic fields presented above indicate that the stiffer phase carries almost all of the stress in the system and that this results in regions of high energy in the stiffer phase, especially when the domains are oriented in the direction of applied strain. It is in such a region that fracture of the stiff B polymer occurs. The continuous domain of stiff B polymer that is aligned in the tensile direction has been severed. The fracture can then spread out in the plane perpendicular to the tensile direction, through the softer A polymer.

The initiation of fracture in a 30:70 system where the softer A phase is dispersed in the stiff B phase matrix is shown in Figure 10c. As the A phase is more compliant, elastic energy concentrations occur about the droplets in the equatorial plane (see Figure 5c). Here, we again show a situation where clustering effects are important since the fracture is initiated in the equatorial plane about two droplets. The fracture extends in the equatorial plane, perpendicular to the tensile direction, around the softer phase material. This system is similar to rubber-toughened polymers where a rubber phase is incorporated into a brittle matrix, and the isolated rubber droplets promote deformation in the matrix by providing a large number of stress concentration sites.[42]

Immiscible polymer blends typically possess weak interfaces, which are susceptible to fracture. Therefore, we consider systems where instead of assuming the characteristics of the interface to be the average of the A and B polymer parameters ("unweakened" interfacial toughness, denoted by w_I^0), we make the toughness of the interface either half ($w_I = 50\%\ w_I^0$) or a quarter ($w_I = 25\%\ w_I^0$) of this unweakened interfacial toughness. Figure 11 shows the damage accumulation in A polymer, B polymer, and interfacial regions for different polymer blend compositions and for different interfacial toughnesses. Making the toughness of the interface 50% less results in systems that are not too dissimilar to those where the interface is unweakened. There is more fracture in the interfacial region, but fracture still predominantly occurs in the bulk regions. In the cases where the toughness of the interface is a quarter of the unweakened interfacial toughness, however, fracture initially occurs at the interfacial regions and continues to be more prevalent along these weak interfaces.

In Figure 12, we consider a local region in which fracture occurs in systems with weak interfaces for the 30:70 and 70:30 mixtures. For the case where the stiff droplets are dispersed in the compliant matrix, the energy concentrations are shown in Figure 5a and are at the poles of the droplets in the tensile direction. In the case where the interface was not weakened, these energy concentrations resulted in the failure of the soft matrix. For the case where the toughness of the interface is a quarter of the unweakened interfacial toughness, fracture is initiated at the interface at the

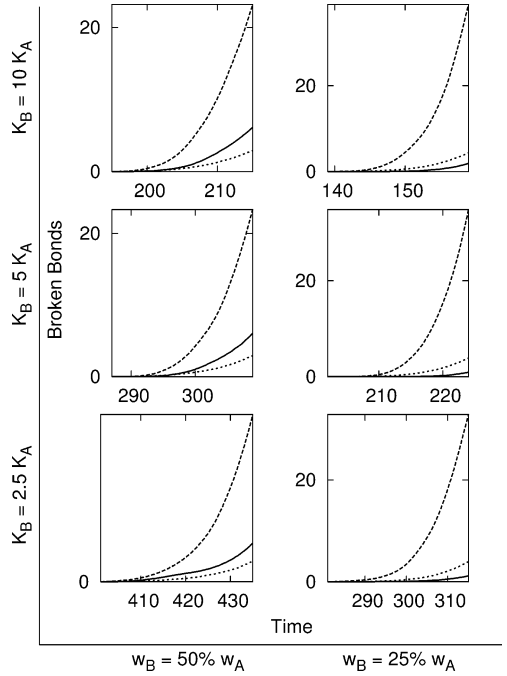

Figure 11. Number of broken bonds ($\times 10^3$) as a function of time for systems with weak interfaces. Broken A bonds (solid lines), B bonds (dashed lines), and interfacial bonds (dotted) are presented for systems where the composition of the polymers varies from 30:70, through 50:50, to 70:30 and where the toughness of the interface is either 50% or 25% that of the unweakened interface.

pole of the particle (Figure 12a). The droplet then decoheres from the surrounding matrix; this has been observed experimentally in polymer blends[43] and is not too disimiliar to the initaion of fracture around glass bead filled polystyrene.[44] Similar to the unweakened interfacial system, clustering effects seem to play a major role. The side of the droplet that decoheres first is the side facing another droplet, which is in close proximity along the tensile direction. This neighboring elastic interaction results in larger elastic energy concentrations and hence a greater probability of interfacial decohesion.

For the case where the soft polymer is dispersed in the stiff polymer matrix (30:70), and the toughness of the interface is a quarter of the unweakened interfacial toughness, the regions at which fracture occurs are depicted in Figure 12b. The soft phase is unable to sustain the same stress as the stiff matrix, and therefore, stress and elastic energy concentrations are found in the equatorial plane about the droplets (see Figure 5c). Figure 12b shows the initiation of fracture in the equatorial plane (perpendicular to the direction of applied strain) at the interface of the droplet. Once sufficient damage has been accumulated at the interface, the fracture spreads out through the stiff matrix as shown by the increase in broken B polymer bonds in Figure 11 for the same system. Local regions of fracture initiation in the systems of 50:50 composition where found to be similar to that of the 30:70 composition.

Figure 13 shows the stress and strain curves for systems with either unweakened interfaces or interfaces where the toughness is either half or a quarter of this unweakened interfacial toughness. In all systems considered here, failure occurs earlier in the systems with weaker interfaces. Because of the greater interfacial area in the bicontinuous systems, we would expect these

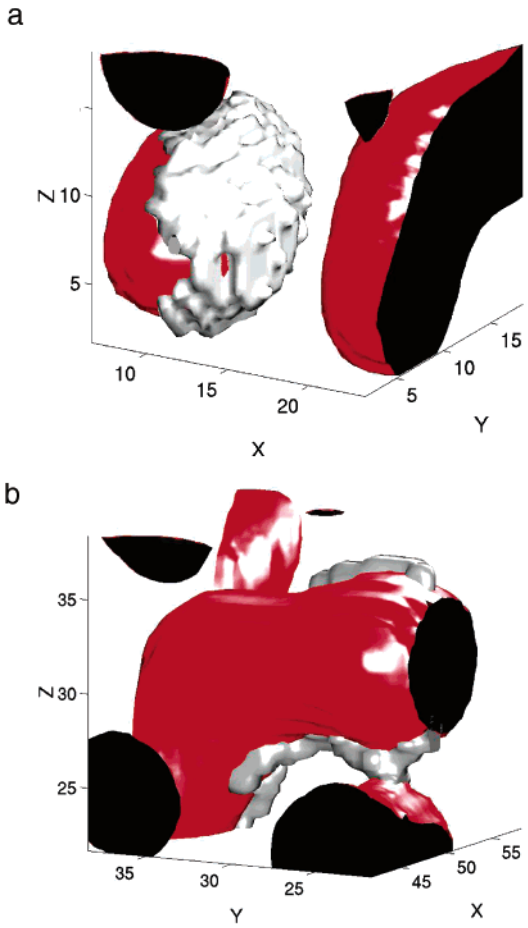

Figure 12. Graphical representation of a typical region of incipient fracture for a system where the stiffness of the B polymer is 10 times that of the A polymer, the toughness of the B polymer is 50% that of the A polymer, and the toughness of the interface is 25% that of the unweakened interface. Systems of (a) 70:30 and (b) 30:70 composition are presented. Deformation is applied in the *x*-direction.

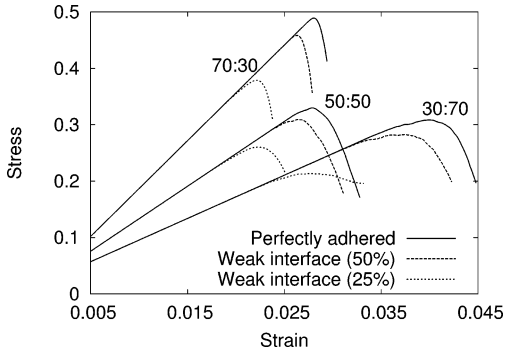

Figure 13. Stress−strain plots for systems of different compositions ranging from systems containing soft dispersed droplets in a stiff matrix, through bicontinuous systems, to systems containing stiff dispersed droplets in a soft matrix. The toughness of the stiffer phase is taken to be 50% that of the softer phase. Unweakened interfaces (averaged from the A polymer and B polymer toughnesses) and weakened interfaces (whose toughnesses are 50% and 25% that of the unweakened interfaces) are considered.

systems to perform poorly, relative to the dispersed systems, as the interface is made weaker. However, the 50:50 system appears to perform worse, in terms of both strength (maximum stress) and toughness (area under the curves), regardless of interfacial weakness. Therefore, the regions of elastic field concentrations, which

are more common in bicontinuous systems of greater interfacial area, play a dominant role in the fracture of polymer blends.

3.3. Comparisons with Experiment. Blending a minority compliant polymer phase with a majority stiff polymer phase offers an attractive route to increasing the ductility and toughness of the brittle polymer without necessarily sacrificing its rigidity and strength.[42] Because rubber has excellent elasticity and toughness, stiff polymers are often toughened through the inclusion of rubber particulates. It should be noted, however, that the stress concentrations surrounding a compliant minority phase particle are similar to the stress concentrations surrounding a void,[45] and the toughening mechanisms are similar.[46] Merz[47] originally proposed the idea that such systems fail through the creation of many microcracks, rather than a single dominating crack, therefore, requiring more elastic energy and resulting in an increase in toughness. Regions of high stress concentration and incipient crack propagation can in fact be ascertained around the compliant domains in Figure 10c and, in further agreement with experimental studies, occur in the equatorial plane of these regions.[42,48]

Bicontinuous blends possess stiffnesses in between the stiffness of both the constituent polymer phases.[49,11] However, the strength and toughness of a bicontinuous blend do not follow this trend and exhibit a minimum in a system of 50:50 compositions.[49] This is considered to be due to the weak interfacial adhesion between the polymers[49,50] and is also observed in the bicontinuous systems considered here (see Figure 13). Furthermore, our results show that the bicontinuous systems perform worse than the dispersed systems regardless of the interfacial adhesion as such systems have more regions of local elastic mismatch and, hence, an increase in the number of stress and strain concentrations.

Dispersing a brittle polymer into a compliant polymer generally results in a composite material with increased stiffness and impact strength relative to the compliant matrix material.[43] However, these composite systems also exhibit a reduction in toughness upon the dispersion of the rigid phase. The composite generally fails through interface decohesion,[43] and the mechanism is similar to the failure of polymers reinforced with glass beads. Dekkers and Heikens[44,52] found that in the case of a poorly adhering sphere decohesion occurs at the poles and continues along the phase boundary. This creates a cap-shaped cavity similar to that seen in Figure 12a. However, in the case of excellent interfacial adhesion, the crazes form near the poles of the glass beads in regions of stress concentration. Qualitatively similar phenomena can also be seen in our systems in Figure 10a, where fracture has occurred near the poles of the dispersed phase in regions of stress concentration.

4. Summary and Conclusions

We investigated the phase separation of binary polymer blends and obtained heterogeneous microstructures where either droplets of one polymer are dispersed in a matrix of the other polymer or both polymers are intertwined in a bicontinuous morphology. We could then consider the deformation and fracture of these specific systems, having to make no assumptions about the mesoscale structure of the mixtures. We focused on the case where one polymer component is both stiffer and weaker than the other.

We determined the local deformation fields in these heterogeneous systems and isolated regions of local elastic field concentrations. We could then compare the locations of fracture initiation and these local deformation fields. For the case of a stiff polymer phase dispersed in a soft polymer matrix, we find that stress and strain concentrations at the poles of the droplets lead to crack initiation in the soft matrix. Incipient fracture in the bicontinuous systems occurs in the stiffer phase, in regions where the domain structure is oriented parallel to the tensile direction. When a soft polymer is dispersed in a stiff polymer, fracture is observed to nucleate in the stiff matrix at the equatorial plane of the droplets.

Immiscible polymer blends generally possess weak interfaces, and therefore, we considered the effects of this weak region on the location and nature of material failure. In the case of substantial interfacial weakening, we find that fracture is initiated at the interfacial regions. In particular, the systems that contain isolated droplets of a stiff polymer in a soft polymer matrix failed through interfacial decohesion, where the droplets separate from the surrounding system. The systems that contain soft polymer droplets dispersed in a stiff polymer matrix also initially failed at the interfacial regions but in the equatorial plane where progressive fracture propagates through either the soft droplets or into the surrounding stiff polymer matrix.

For all the systems we considered here, regions of incipient fracture are associated with elastic field concentrations due, in part, to clustering effects. For example, in the case of a dispersed stiff polymer phase being weakly bonded to the surrounding soft polymer matrix, fracture is initiated via interfacial decohesion. This debonding is found to occur at the pole of a droplet. However, this occurs predominantly at a droplet pole that is facing, and in close proximity to, another droplet. This is consistent with experimental studies where fracture toughness is known to depend on surface−surface interparticle spacings.[43]

The work presented here offers a computationally efficient method of simulating the deformation and fracture of heterogeneous systems. However, the current study was limited to linear elastic, perfectly brittle constituents. It should be noted that plastic deformation has been included in the LSM by decreasing the elastic moduli locally while maintaining stress continuity.[7] Studies involving such plastic deformation have yielded the required differential response of the stress−strain curve in an isotropic manner, but the deformation was not volume conserving (the Poisson's ratio was still limited to an upper bound of 1/4). The LSM has also been modified to incorporate a viscoelastic response;[9] here, the system was assumed to consist of a Kelvin unit in series with an elastic unit. The LSM can, therefore, accurately capture the nonlinear deformation of polymeric materials but is in general limited to a Poisson's ratio of 1/4. This limitation is a consequence of the connectivity of the bonds; here, only pairwise harmonic interactions are considered, and the resultant elastic constants, therefore, satisfy the Cauchy relations.[53] Attempts to rectify this problem in classic molecular dynamics led to many-body potentials being considered, such as a volume-dependent term[54] or the embedded atom method.[55,56] Recently, Gusev[57] has mapped a variant of the LSM onto the finite element method, which does not possess the same upper bound for the

Poisson's ratio and opens up the possibility of incorporating nonlinearity and anisotropy (and, therefore, the possibility of explicitly incorporating "crazed" elements[24]). The work presented here, however, does not include such nonlinear deformation mechanisms and, as mentioned, is limited to a Poisson's ratio of 1/4. The current study does not, therefore, account for global ductility or the production of local shear bands. Also, the Poisson's ratio in polymeric materials is typically between 1/3 and 1/2, as opposed to 1/4 in the systems considered here. However, stress and strain concentrations are more likely to occur as a consequence of the local mismatch in Young's modulus and not the local variations in Poisson's ratio. Therefore, the regions of high deformation and incipient fracture in our simulations are representative of real polymer systems, and the results presented here appear to be in qualitative agreement with experimental observations (see section 3.3).

In conclusion, we show that computer simulations can provide an efficient method for studying the deformation and fracture of complex heterogeneous materials, such as polymer blends, and enable us to visualize the complex elastic fields and regions of incipient fracture. These studies, therefore, provide additional insight into the initiation and propagation of fracture and can be instrumental in the understanding and design of novel structural materials.

Acknowledgment. The authors gratefully acknowledge financial support from the DOE.

References and Notes

(1) Ryan, A. J. *Nat. Mater.* **2002**, *1*, 8.
(2) *Encyclopaedic Dictionary of Commercial Polymer Blends*; Utracki, L. A., Ed.; ChemTec Publishing: Toronto, 1994.
(3) *Commercial Polymer Blends*; Utracki, L. A., Ed.; Chapman and Hall: London, 1998.
(4) Cahn, J. W.; Hilliard, J. E. *J. Chem. Phys.* **1958**, *28*, 258−267.
(5) Cahn, J. W. *J. Chem. Phys.* **1965**, *42*, 93−99.
(6) Monette, L.; Anderson, M. P. *Modell. Simul. Mater. Sci. Eng.* **1994**, *2*, 53−66.
(7) Buxton, G. A.; Cleaver, D. J.; Care, C. M. *Modell. Simul. Mater. Sci. Eng.* **2001**, *9*, 485−497.
(8) Monette, L.; Anderson, M. P.; Wagner, H. D.; Mueller, R. R. *J. Appl. Phys.* **1994**, *75*, 1442−1455.
(9) Buxton, G. A.; Balazs, A. C. *J. Chem. Phys.* **2002**, *117*, 7649−7658.
(10) Buxton, G. A.; Balazs, A. C. *Phys. Rev. E* **2003**, *67*, 031802−031813.
(11) Buxton, G. A.; Balazs, A. C. *Interface Sci.* **2003**, *11*, 175−186.
(12) *Statistical Models for the Fracture of Disordered Media*; Herrmann, H. J., Roux, S., Eds.; Elsevier Science: Amsterdam, 1990.
(13) Meakin, P. *Science* **1991**, *252*, 226−234.
(14) Ostoja-Starzewski, M.; Sheng, P. Y.; Jasiuk, I. *Eng. Fract. Mech.* **1997**, *58*, 581−606.
(15) Alzebdeh, K.; Al-Ostaz, A.; Jasuik, I.; Ostoja-Starzewski, M. *Int. J. Solids Struct.* **1998**, *35*, 2537−2566.
(16) Rautiainen, T. T.; Alava, M. J.; Kaski, K. *Phys. Rev. E* **1995**, *51*, R2727−R2730.
(17) Pla, O.; Guinea, F.; Louis, E.; Ghaisas, S. V.; Sander, L. M. *Phys. Rev. B* **1998**, *57*, R13981−R13984.
(18) Pla, O.; Guinea, F.; Louis, E.; Ghaisas, S. V.; Sander, L. M. *Phys. Rev. B* **2000**, *61*, 11472−11486.
(19) Buxton, G. A.; Balazs, A. C. *Phys. Rev. B* **2004**, *69*, 054101−054104.
(20) Rottler, J.; Barsky, S.; Robbins, M. O. *Phys. Rev. Lett.* **2002**, *89*, 148304−148307.
(21) Rottler, J.; Robbins, M. O. *Phys. Rev. E* **2003**, *68*, 011801−011818.
(22) Hui, C. Y.; Ruina, A.; Creton, C.; Kramer, E. J. *Macromolecules* **1992**, *25*, 3948−3955.
(23) Sha, Y.; Hui, C. Y.; Kramer, E. J. *J. Mater. Sci.* **1999**, *34*, 3695−3707.
(24) Socrate, S.; Boyce, M. C.; Lazzeri, A. *Mech. Mater.* **2001**, *33*, 155−175.
(25) Laradji, M. *J. Phys.: Condens. Matter* **1992**, *4*, 6715−6728.
(26) Good, K.; Kuksenok, O.; Buxton, G. A.; Ginzburg, V. V.; Balazs, A. C. *J. Chem. Phys.* **2004**, *121*, 6052−6063.
(27) Elder, K. R.; Rogers, T. M.; Desai, R. C. *Phys. Rev. B* **1988**, *38*, 4725−4739.
(28) Oono, Y.; Puri, S. *Phys. Rev. Lett.* **1987**, *58*, 836−839.
(29) Oono, Y.; Puri, S. *Phys. Rev. A* **1988**, *38*, 434−453.
(30) Shinozaki, A.; Oono, Y. *Phys. Rev. E* **1993**, *48*, 2622−2654.
(31) Verlet, L. *Phys. Rev.* **1967**, *159*, 98−103.
(32) Tuckerman, M.; Berne, B. J.; Martyna, G. J. *J. Chem. Phys.* **1992**, *97*, 1990−2001.
(33) Griffith, A. A. *Philos. Trans. R. Soc. London* **1920**, *A221*, 163.
(34) Monette, L.; Anderson, M. P.; Ling, S.; Grest, G. S. *J. Mater. Sci.* **1992**, *27*, 4393−4405.
(35) Curtin, W. A.; Pamel, M.; Scher, H. *Phys. Rev. B* **1997**, *55*, 12051−12061.
(36) The current study considers the mechanics of the system to be represented by continuum elasticity. We, therefore, assume that we are simulating the deformation at a length scale greater than that of microscopic phenomena (such as crazing, which occurs at a length scale on the order of μm[37,38]). This introduces an inherent length scale to the lattice spacing, $\Delta x > 10^{-6}$ m. This length scale, therefore, corresponds to the typical length scale of the domain structure. Since our simulation box is $L^3 = 64^3$, the length scale of the entire simulations is therefore $>10^{-5}$ m. Having established a length scale, we can now obtain a time scale by considering the speed of sound in the material. If we assume a speed of sound of 1600 m s^{-1} (e.g., as that in rubber), then we can obtain a time scale $\Delta t > 10^{-9}$ s through a comparison with the speed of sound in our simulations, $c_s = \sqrt{3k/M} \sim$ unity. The strain rate in the simulations presented here is $\dot{u} = 1.56 \times 10^{-4}$ in dimensionless units; this is $<10^4$ s^{-1} in real units (a high strain rate in the region 10^2−10^4 s^{-1} corresponds to that of hydraulic or pneumatic test methods[39]).
The Young's modulus of polymers is typically of the order of 10^9 N m^{-2}, while in the dimensionless units used here, the typical Young's modulus was 10. Therefore, the maximum normal stress in Figure 3a−c of 0.5 corresponds to ∼50 MPa (note that strain is dimensionless and, consequently, the ratio of stress and elastic modulus is the same in real units and dimensionless units). In a similar manner, the maximum energy in Figure 5a−c of 15×10^{-3} corresponds to ∼1500 kJ m^{-3}. (Note that these values are typical for polymer materials prior to fracture.[39])
(37) Beahan, P.; Bevis, M.; Hull, D. *Philos. Mag.* **1971**, *24*, 1267−1279.
(38) Beahan, P.; Bevis, M.; Hull, D. *J. Mater. Sci.* **1972**, *8*, 162−168.
(39) *Fracture Behaviour of Polymers*, Kinloch, A. J., Young., R. J., Eds.; Applied Science Publishers: London, 1983.
(40) Seitz, J. T. *J. Appl. Polym. Sci.* **1993**, *49*, 1331−1351.
(41) Regions of high stresses and strains near a spherical particulate are often described by analogy to planetary geometry. In particular, the poles of the particle are the regions which lie near the interface away from the center of the particulate in the direction of applied deformation. The equatorial regions of the particle are regions which are near the interface in a plane which passes through the center of the particle and is perpendicular to the direction of applied deformation.
(42) *Polymer Blends;* Paul, D. R., Bucknall, C. B., Eds.; John Wiley and Sons: New York, 2000; Vol. 2.
(43) Evans, R. D.; MacGillivray, L. A.; Boyd, J. D.; Baker, W. E.; Pith, T. *Polym. Networks Blends* **1996**, *6*, 181−187.
(44) Dekkers, M. E. J.; Heikens, D. *J. Mater. Sci.* **1983**, *18*, 3281−3287.
(45) Smit, R. J. M.; Brekelmans, W. A. M.; Meijer, H. E. H. *J. Mater. Sci.* **2000**, *35*, 2869−2879.
(46) Bagheri, R.; Pearson, R. A. *Polymer* **1995**, *25*, 4883−4885.
(47) Merz, E. H.; Claver, G. C.; Baer, M. *J. Polym. Sci.* **1956**, *22*, 325−341.
(48) Cawse, J. L.; Stanford, J. L.; Still, R. H. *Polymer* **1987**, *28*, 368−374.
(49) Barentsen, W. M.; Heikens, D. *Polymer* **1973**, *14*, 579−583.
(50) Fayt, R.; Jerome, R.; Teyssie, P. *J. Polym. Sci., Polym. Phys. Ed.* **1981**, *19*, 1269−1272.

(51) Kelner, I. Stephan, M.; Jakisch, L.; Fortelny, I. *J. Appl. Polym. Sci.* **1999**, *74*, 1404−1411.
(52) Dekkers, M. E. J.; Heikens, D. *J. Mater. Sci., Lett.* **1984**, *3*, 307−309.
(53) *Dynamical Theory of Crystal Lattices*; Born, M., Huang, K., Eds.; Oxford University Press: Oxford, 1954.
(54) Johnson, R. A. *Phys. Rev. B* **1972**, *6*, 2094−2099.
(55) Daw, M. S.; Baskes, M. I. *Phys. Rev. Lett.* **1983**, *50*, 1285−1288.
(56) Daw, M. S.; Baskes, M. I. *Phys. Rev. B* **1984**, *29*, 6443−6453.
(57) Gusev, A. A. *Phys. Rev. Lett.* **2004**, *93*, 034302−034305.

MA048470R